Stress-induced pop-in and pop-out nanoindentation events in CuAlBe Shape Memory Alloys

C Caër, E Patoor, S Berbenni, J-S Lecomte

Stress analysis by nanoindentation of “pop-in” and “pop-out” events in CuAlBe Shape Memory Alloys

Célia Caër, Etienne Patoor, Stéphane Berbenni, Jean-Sébastien Lecomte

Laboratoire d’Étude des Microstructures et de Mécanique des Matériaux (LEM3), UMR CNRS 7239, Université de Lorraine, Arts et Métiers ParisTech, 57070 Metz, France

Abstract

Over the last thirty years martensitic transformation of Shape Memory Alloys (SMA) has been widely studied from micro to macro scale. However the models developed to predict SMA behavior give a simplified description of martensite variant forming mechanisms under thermomechanical loading. These approaches are mean field models which approximate continuously the internal characteristics of a grain without taking into account discrete variant activation mechanisms. This study aims at modeling and characterizing martensitic transformation at the nanometric scale. A discrete variant activation mechanism, characterized by the presence of pop-in and pop-out events on the nanoindentation curve is observed and analyzed. A model of plasticity nucleation is adapted to the activation of martensitic transformation in SMA by the development of an indentation “Patel and Cohen” factor.

Keywords: Nanoindentation, martensitic phase transformation, SMA, pop-in, pop-out, stress analysis

1. Introduction

Shape Memory Alloys (SMA) can undergo a reversible thermoelastic martensitic phase transformation. This is due to a displacive, diffusionless, first order phase transition. SMA can show a specific behavior called superelasticity which is associated with a stress induced strain transformation. When the material is loaded at some specific constant temperature the austenitic parent phase undergoes a stress-induced phase transformation from austenite to martensite and large amounts of inelastic strains are developed. Upon unloading back to the zero stress state the material undergoes a reverse phase transformation from martensite back to austenite and all the inelastic deformations are recovered [1].

Instrumented indentation is widely used to study material’s mechanical properties such as hardness and Young’s Modulus at small scales. This technique is also very useful to characterize discrete mechanisms at the nanometer scale such as homogeneous dislocation nucleation [2], oxide breaking [3], microcracking [4] and phase transformation. Incipient plasticity has been characterized on a wide range of materials by the appearance of an excursion event, called pop-in, on the loading of the nanoindentation curve. Phase transformation was observed by Woirgard et al. [5] on a silicon single crystal, as the appearance of a displacement burst during the unloading of the nanoindentation curve, called pop-out. This excursion event was explained as phase transformation as neither slip lines associated to incipient plasticity nor microcracks could be observed around the indenter.

Applied to superelastic SMA the nanoindentation technique is an experimental way of investigating their thermomechanical properties and their evolution with heat treatments [6], but also to study the martensitic transformation at the nanometer scale. This completely reversible phase transition is characterized on the nanoindentation curve by the appearance of displacement bursts during both loading and unloading and by zero residual strain after complete unloading. Martensitic phase transformation has been mostly studied using nanoindentation in NiTi SMA [7] [8] [9] and a few studies have been led on superelastic CuAlNi [10] [11]. NiTi alloys are not the best candidates to

study martensitic transformation at small scale because in these alloys the phase transition is usually coupled with plasticity [12] and it is then difficult to distinguish the two mechanisms. However Frick et al. [13] have observed discrete phase transition on shape memory and superelastic NiTi alloys using nanoindentation. The present study focuses on CuAlBe SMA because the addition of beryllium in interstitial solid solution hardens the matrix and increases the plastic yield stress of the parent phase, favouring phase transition activation limiting plasticity nucleation [14]. One of the objectives of this paper is to show evidence of discrete phase transition at the nanometer scale in CuAlBe shape memory alloy identified by "pop-in" and "pop-out" events.

Whereas martensitic transformation has been investigated using nanoindentation, few efforts have been made to model this phase transition under such testing conditions.Pfetzing-Micklich et al. [15] modelled martensitic transformation in NiTi SMA using molecular dynamics, however this numerical technic is time-consuming and difficult to set up. This study proposes a simple criterion predicting the activation of the first martensite variant as a function of crystallographic orientation.

This paper is organized as follows. In section 2, Nickel and CuAlBe specimens used in this study are presented. Both surface preparation and nanoindentation experimental procedure are detailed for each material. In section 3, equations related to the stress field calculation of nanoindentation of a linear isotropic elastic half-space with an axisymmetric indenter are presented. The indentation Schmid factor is recalled and a new criterion for martensitic transformation activation under nanoindentation loading, the indentation "Patel and Cohen" factor is introduced. In section 4, nanoindentation tests performed on several crystallographic orientation of the Nickel specimen are presented and compared to the computed indentation Schmid factor, in order to validate both stress field computation and experimental procedure. Finally, nanoindentation curves for different crystallographic orientations of the CuAlBe SMA specimen are presented, discussed, and compared to the computed indentation "Patel and Cohen" factor.

2. Experimental

A polycrystalline plate of shape memory alloy CuAlBe (Cu-12wt%Al-0.5wt%Be) was used in the present investigation. The specimen exhibits the following transformation temperatures: Ms = 269 K, Mf = 279 K, As = 243 K and Af = 265 K (respectively martensite start and finish and austenite start and finish). The sample is initially in the austenitic state (FCC structure) at room temperature and shows a superelastic behavior. Theaverage grain size of the specimen is about one millimeter which is large enough according to the indenter size to allow considering the behavior of the indented grain as the behavior of a single crystal. A polycrystalline sample of commercially pure FCC Nickel (>99,99%) wasalso used in this study to validate the experimental procedure. The grain size of the Ni specimen is around 140 µm.
Both specimens were first mechanically polished with decreasing SiC paper and particulate diamond paste. The final mechanical polish was performed with a 1 µm diamond paste. Finally they were electropolished in a solution of ($C_2H_5OH(25mL) + H_3PO_4(25mL) + H_2O$) with a DC voltage of 20 V for CuAlBe and in a solution of (H_2SO_4 (20 mL) + $CH_3OH(80mL)$) with a DC voltage of 35 V for the Nickel specimen. Prior the nanoindentation tests EBSD mappings were performed in order to determine the crystal orientation of the grains.
Nanoindentation tests were conducted using a commercial CSM Instruments nanoindenter "NHT2". This device is fitted with a reference ringtaking the depth reference directly on the specimen surface, so avoiding the user to wait hours for thermal drift stabilization.Tests were performed using two Berkovich tips. The radius of curvature of the indenter tips were estimated on the basis of AFM measurementsto be approximately 300 nm for the tip used on Nickel and 1 µm for the indenter used on the CuAlBe specimen.
Nanoindentation tests were performed on Nickel on 4 grains A_1, A_2, A_3 and $A_4$with a crystal orientation respectively close to [001], [101], [111] and [123], and on three grains B_1, B_2 and B_3 of CuAlBe with an orientation close to [001] and [111] .

Distinct nanoindentation procedures were set up for CuAlBe and Nickel. For both materials nanoindentation tests were performed under load control with a constant rate of $\dot{P}/P = 0.125\ s^{-1}$for Nickel and$\dot{P}/P = 0.01\ s^{-1}$for CuAlBe. In the case of the superelastic SMA, due to the superelastic behavior of the material and the absence of residual strain (no plastic deformation) after a nanoindentation test, it is then possible to perform several indentations at the same location considering each test independently from others. So for SMA the loading test sequence was made up of four loading-unloading cycles up to 100 µN for grains B_1 and B_2 and 500 µN for grain B_3. The minimum load between two consecutive cycles was set to2 µN to keep contact between the Berkovich indenter tip and the specimen surface. The aim of the first cycle is to break the oxide layer, and the data from the three following cycles were used for the study. These cycles of loading-unloading at the same position are not relevant for tests on Nickel, were irreversible plasticity is produced. Nanoindentation tests on this material were set up of a unique cycle of loading-unloading up to a maximum load of 800 µN. Indentations were operated at sufficient distance from the grain boundary to avoid any interaction between the stress field generated by the indentation and the incompatibility stresses associated to the presence of a grain boundary. For tests performed on Nickel a distance of 30 µm was respected between each indentation to avoid any interaction between the incompatibility stresses and stresses generated within the crystal by the indent load.

3. Theory

3.1. Hertzian elastic contact

Using elastic Hertzian theory of a sphere in contact with a semi-infinite half space, the equation used to illustrate the idealized elastic contact was:

$$P = \frac{4}{3} E_r \sqrt{R\, h^3} \tag{1}$$

where P is the applied load, h the penetration depth, R the radius of the indenter tip and Er the reduced modulus. As nanoindentation is a local experimental technic, it may be relevant to integer the material anisotropy to the reduced modulus. The anisotropic elastic reduced modulus is related to the elastic isotropic modulus E_i and Poisson ratio ν_i of the indenter and to the effective indentation moduli of the specimen, and defined as:

$$\frac{1}{E_r} = \frac{1-\nu_i^2}{E_i} + \frac{1}{E_{eff}^{(hkl)}} \tag{2}$$

This effective indentation modulus is computed from the expression given by Vlassak and Nix [16]:

$$E_{eff}^{(hkl)} = \beta_{(hkl)} \left(\frac{E_s}{1-\nu_s}\right)_{isotropic} \tag{3}$$

Where $\beta_{(hkl)}$ is a term related to the crystal orientation and the anisotropy factor of the sample andE_s and ν_s are respectively the isotropic Young's modulus and Poisson's ratio of the specimen. Values taken for the isotropic elastic constants were $E_s^{Ni} = 192{,}5$ GPa and $\nu_s^{Ni} = 0{,}33$ [17] for Nickel and $E_s^{CuAlBe} = 78$ GPa and $\nu_s^{CuAlBe} = 0{,}3$ [14] for CuAlBe. The anisotropy factor A depends on the material elastic constants: $A = 2c_{44}/(c_{11} - c_{12})$.

These constants are $c_{11} = 244$ GPa, $c_{12} = 158$ GPa and $c_{44} = 102$ GPa for Nickel [18] and $c_{11} = 138$ GPa, $c_{12} = 124$ GPa and $c_{44} = 93$ GPa for CuAlBe [19]. Finally the anisotropy factor of respectively Nickel and CuAlBe are $A_{Ni} = 2{,}4$and $A_{CuAlBe} = 13$. Vlassak and Nix's table was used for CuAlBe although it is made up for anisotropy factors contained between 0.8 and 8. Resulting effective modulus and reduced modulus for the [001], [101] and [111] of Nickel and [001] and [111] of CuAlBe are presented in Table 1.

Grain	A_1	A_2	A_3	B_1 and B_2	B_3
E_{eff}(GPa)	204	220	225	72	97
E_r (GPa)	173	185	188	68	89

Table 1 : Effective modulus and reduced modulus for grains A_1, A_2 A_3 of Nickel and grains B_1, B_2 and B_3 of CuAlBe.

As Vlassak and Nix's tables only gives effective modulus for [001], [101] and [111] orientations, the reduced modulus under anisotropic elasticity hypothesis for grain A_4 with a [123] orientation could not be computed.

3.2. Indentation stress field

The stress field due to an axisymmetric indenter under the hypothesis of linear isotropic elasticity was determined from integrals adapted from equations (3.19) of Johnson [20]. The stress field due to an indentation loading is not homogeneous, unlike pure uniaxial compression. The integrals were computed thanks to a Gauss-Legendre integration procedure. The ratio of the stress components at some arbitrary position (x,y,z) to the maximum contact pressure p_0 were computed according to:

$$\frac{\sigma_{ij}(x_1,x_2,x_3)}{p_0} = \int_0^a \int_0^{2\pi} \tilde{p}(x_1',x_2')\widetilde{\sigma_{ij}}(x_1-x_1',x_2-x_2',x_3)dx_1'dx_2' \tag{4}$$

where $x_1' = r\cos\theta$, $x_2' = r\sin\theta$, a is the contact radius and the stress components $\widetilde{\sigma_{ij}}$are due to a point contact (detailed in annexe A).The surface pressure distribution $\tilde{p}$for a circular contact is given by :

$$\tilde{p}(x_1',x_2') = \sqrt{1-\left(\frac{x_1',x_2'}{a}\right)^2} \tag{5}$$

At the first stages of the loading, the stress field under the indenter firstinduces elastic strain, and with the increasing of the applied load, other types of deformation such as plastic strain or transformation strain are activated.

3.3. Indentation Schmid Factor for plasticity

When a loading path is applied to a material showing an elasto-plastic behavior,the first material response is elastic up to a yield point at which plasticity nucleation starts. The plastic strain adds to the elastic strain, and takes the form:

$$\varepsilon_{ij}^{P(v)} = \gamma R_{ij}^{(v)} \tag{6}$$

whereγ is the slip magnitude and R_{ij} is the Schmid tensor, expressed as follows:

$$R_{ij}^{(v)} = \frac{1}{2}\left(n_i^{(v)}s_j^{(v)} + n_j^{(v)}s_i^{(v)}\right) \tag{7}$$

wheren and s are respectively the slip normal and the slip direction of the slip system (v), the Latin subscripts running from 1 to 3.

The resolved shear stress $\tau_R^v$is the product of the plastic strain and the stress field, it consequently depends on the position in the interface and on the considered slip system (v) running from 1 to the number of slip systems:

$$\tau_R^{(v)}(x,y,z) = \varepsilon_{ij}^{P(v)}\sigma_{ij}(x,y,z) \tag{8}$$

To determine the influence of crystallographic orientation on the initial yield point under Hertzian contact, Li et al. [16]introducedthe notion of indentation Schmid factor defined as the ratio of the maximum resolved shear stress to the maximum contact pressure:

$$S = \frac{1}{p_0} \max_{(v),x,y,z} \tau_R^{(v)}(x,y,z) \quad (9)$$

As a usual Schmid factor, the indentation Schmid factor predicts the activation of plasticity. The higher this criterion, the lower the critical load for dislocation activation.

3.4. Indentation "Patel and Cohen" Factor for martensitic transformation

Mechanical loading of Shape Memory Alloys induces martensitic transformation before any plastic deformation happens. Thisphase transformation is due to a transformation strain which adds to the elastic strain and takes the form[21]:

$$\varepsilon_{ij}^{T(v)} = gR_{ij}'^{(v)} \quad (10)$$

Where g is the displacement magnitude and R'_{ij} is the Patel and Cohen tensor [22], expressed as follows:

$$R_{ij}'^{(v)} = \frac{1}{2}\left(n'^{(v)}_i m_j^{(v)} + n'^{(v)}_j m_i^{(v)}\right) \quad (11)$$

where n' and m are respectively the normal to the habit plane and the direction of transformation of the variant (v). Unlike the slip direction for plasticity, the direction of transformation is not contained in the habit plane.

The driving force for martensite activation may be expressed as a function of the transformation strain, the stress field and a term related to the chemical energy:

$$F_d^{(v)}(x,y,z) = \varepsilon_{ij}^{T(v)}\sigma_{ij}(x,y,z) + B(T - T_0) \quad (12)$$

whereT is the room temperature, T_0 is the equilibrium temperature at which the volume fraction of austenite equals the volume fraction of martensite, T_0 and B arematerial constants.

As the term $B(T - T_0)$ is a material constant, depending nor on the position under the indenter neither on the considered variant, it may be neglected in the calculation of the driving force:

$$F_d^{(v)}(x,y,z) = \varepsilon_{ij}^{T(v)}\sigma_{ij}(x,y,z) \quad (13)$$

The condition for a variant of martensite to appear in austenite is that the driving force of this variant reaches a critical load F_c: $F_d = F_c$. By analogy to dislocation nucleation a criterion to determine the activation of martensitic transformation under nanoindentation loading called indentation "Patel and Cohen" factor S_{PC}has been developed in this study:

$$S_{PC} = \frac{1}{p_0} \max_{(v),x,y,z} F_d^{(v)}(x,y,z) \quad (14)$$

Where F_d is computed from the indentation contact stress field. Equation 14not only permits the calculation of the indentation "Patel and Cohen" factor, but also the determination of the first martensite variant to appear under the indenter and the position of the activation of this variant.

4. Results and discussion

4.1. Dislocationactivation in Nickel

The Schmid and Boas'sconvention for slip systems of FCC slip systems were used for computations on Nickel. The Schmid factor was first calculated from equation (8) for tensile and compression loadings of Nickel. The resulting inverse pole figures, for both uniaxial deformation of Ni, were similar and showed a repartition of Schmid factors along concentric ellipses. Using equation (9) and the contact stress field, the indentation Schmid factor has been computed and its variation with

crystallographic orientation is represented on Figure 1 on an inverse pole figure. Indentation Schmid factor distribution, form a set of concentric circles as opposed to the ellipses of the uniaxial loading case. At the centre of these circles, close to a [123] crystal orientation, is the maximum indentation Schmid factor, whereas the minimum indentation Schmid factor is close to the [111] crystal orientation.

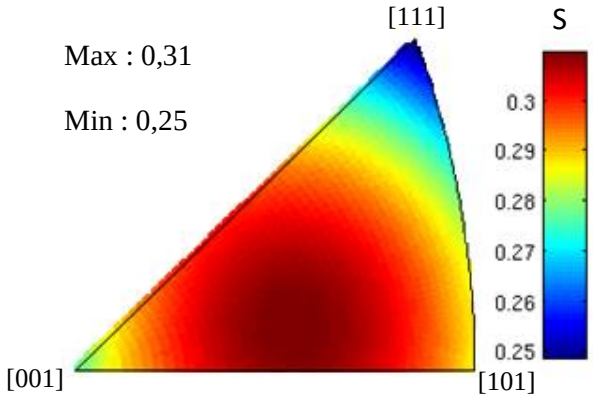

Figure 1 : Inverse pole figure of the indentation Schmid factor S defined as the ratio of the maximum shear stress to the maximum contact pressure plotted for Ni single crystal with FCC structure and [111]<0$\bar{1}$1> slip systems.

The repartition of the indentation Schmid factors in the inverse pole figure is similar to the one found by Li et al. under the hypothesis of an elastically anisotropic solid and the criterion values are slightly higher but still very close to Li et al's. As our calculation was made under the hypothesis of an elastically isotropic solid, this correlationshows that anisotropic elasticity is not necessary at the first order. It also validates ourcontact stress field computation.

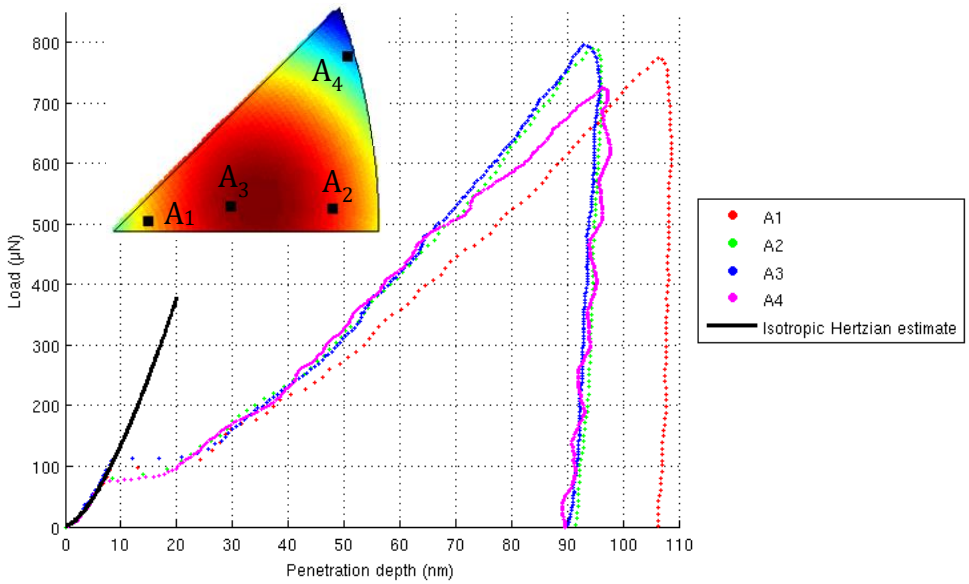

Figure 2: Representative load-displacement nanoindentation curve for the grainsA_1, A_2, A_3 and A_4 of the Nickel specimen with orientations respectively close to [001], [101], [111] and [123] and a Hertzian estimate (dashed line).

Figure 2 shows typical nanoindentation curves on Nickel using a Berkovich indenter. The first part of the loading curves can be very well described by the anisotropic Hertzian curves, calculated from the effective modulus. However, for a better understanding of figure 2, the isotropic Hertzian estimate was plotted instead of these anisotropic Hertzian curves, and gives a pretty convenient estimate of the first elastic regime. A clear excursion event may be observed on each curve at loads of ~100 ± 20 µN. Plasticity nucleation is evident according to the large residual strain observed after unloading. Similar P-h curves have been obtained by different authors for different orientations of Nickel [23] [24], which means that the experimental procedure used in this study is relevant for the study of excursion events. Also shown in Figure 2 is a dependence of the pop-in activation load to the crystallographic

orientation. The onset of the displacement burst is higher for the [111] orientation, a slightly lower for the [100] orientation and seems to reach a minimum for a crystal orientation close to [101] and [123].
Table 2 presents the average critical load for plasticity activation versus the computed Schmid factor for the four studied crystallographic orientations. The critical pop-in loads in the table correspond to an average made on six nanoindentation tests for grains A_1 and A_2, and on 13 tests for grains A_3 and A_4.These average critical pop-in loads are in good agreement with Lawrence et al.'s nanoindentation tests performed on pure Nickel with a 100 nm radius tip. The authors found the following ranging of the pop-in loads: $F_{PI}^{orientation}$: $F_{PI}^{111} > F_{PI}^{100} > F_{PI}^{101}$.

Crystal orientation	Average critical pop-in load	Indentation Schmid factor
[123]	92,5	0,31
[101]	94,2	0,30
[001]	100	0,29
[111]	142	0,26

Table2 : Average critical pop-in load and computed indentation Schmid factor for the [001], [101], [111] and [123] crystallographic orientations of Nickel.

Plotting Table 2 shows a linear dependence between the average critical pop-in load and the indentation Schmid factor. Clearly, the higher the indentation Schmid factor, the lower the critical load for pop-in activation.
This relation between theory and experiments suggests the relevance of the indentation Schmid factor notion. This also validates the use of our nanoindentation device for the observation of discrete pop-in mechanisms.

4.2. Martensitic transformation activation in CuAlBe

Martensitic transformation in CuAlBe is the transformation from a FCC austenite structure to a 18R martensite crystal. Martensite may appear under the form of 24 variants characterized by their habit plane normal n', displacement direction m and displacement magnitude g. These parameters may be calculated by adapting the theory of Wechsler and al. [26] on martensitic transformation to CuAlBe alloys (De Vos, 1978)[27]. Values used for n', m and g in this study are those proposed by Siredey et al. [21]: $g = 0.22, \{a_n, b_n, c_n\}$ is $\{0.168, 0.688, 0.705\}$ and $\{a_m, b_m, c_m\}$ is $\{0.121, 0.678, 0.725\}$.
From these parameters the transformation strain may be computed for the 24 martensite variants. The driving force for martensitic transformation may then be calculated, using the appropriate stress field. Maxima of the driving force for uniaxial tests on CuAlBe are represented in the inverse pole figures, figure 3.

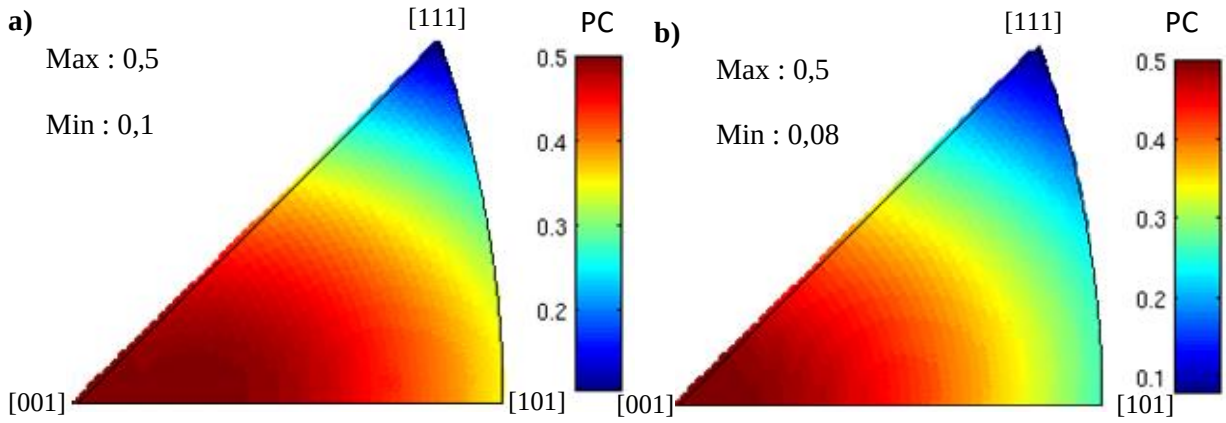

Figure 3: Inverse pole figure the distribution of driving force maxima for a CuAlBe single crystal with FCC structure under a) tensile b) compressive loading paths.

A clear asymmetry of the material behavior is observed between tensile and compressive loading paths. This phenomenon has been explained by Patoor et al. [28] as a loss of symmetry between the austenitic parent phase and the orthorhombic martensitic phase, due to the phase's morphology. This low symmetry of the martensitic phase implies transformation strains, so the activation criterion, to

depend on the loading path. As a consequence different variants are activated whether the loading is traction or compression.
The Patel and Cohen factors range from 0.1 to 0.5 for a tensile test whereas from 0.08 to 0.5 for a compressive loading path.
Figure 4 shows the indentation Patel and Cohen factors distribution in an inverse pole figure.

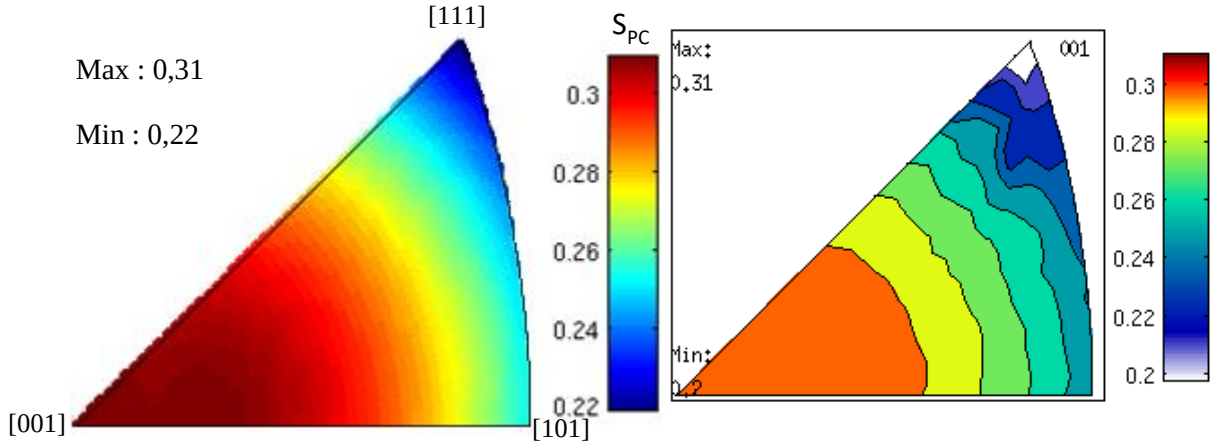

Figure 4: Inverse pole figure representing the indentationPatel and Cohen factor S_{PC} plotted for CuAlBe single crystal with FCC structure.

The indentation Patel and Cohen factors distribution on the inverse pole figure seems to form a set a concentric circles with a maximum at the center, close to the [001] direction, as opposed to ellipses for uniaxial loading.

Nanoindentation tests on CuAlBe were performed at lower maximum loads than tests led on Nickel. It has been observed on NiTi SMA that pop-in events due to phase transformation occur at very low forces, under 80 µN [9]. Furthermore studies on CuAlNi, another copper-based SMA, have shown that small pop-in displacements due to martensitic transformation occur under a load level of 300 µN [19]. This is why the maximum load used for nanoindentation tests performed on [001] oriented CuAlBe wasset to 100µN. According to figure 4, the critical load for phase transformation activation of a [111] oriented CuAlBe should be greater than the one needed to activate martensite in a [001] oriented austenite. This is why the max load was set to 500 µN for tests performed on grain B_3.

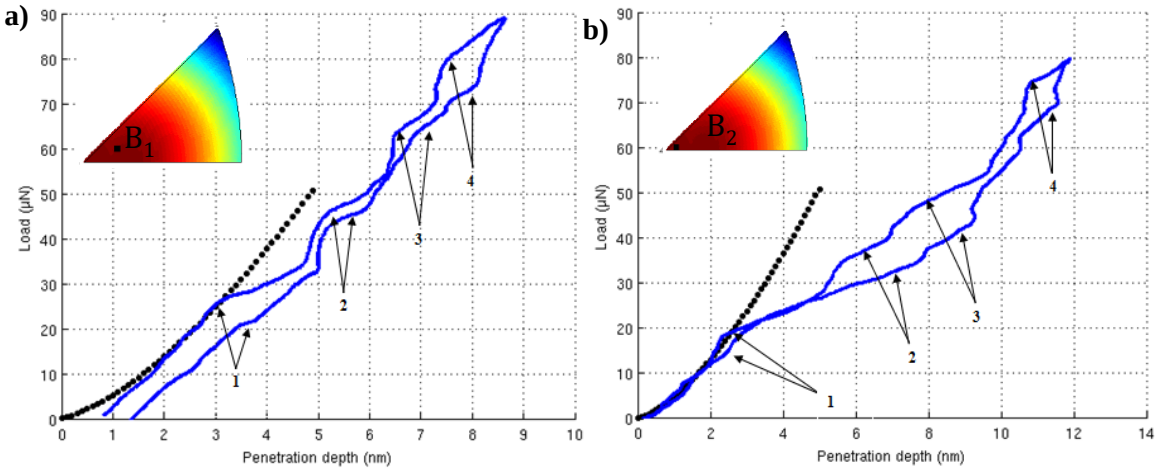

Figure 5: Resulting P-h curve of a nanoindentation test performed on the grains $B_1$and $B_2$with a crystal orientation close to [001] of the superelastic CuAlBe specimen and a Hertzian estimate (dashed line).

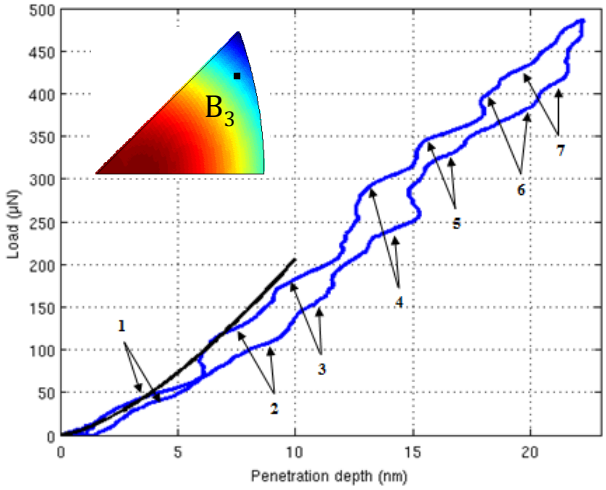

Figure 6: Resulting P-h curve of a nanoindentation test performed on the grain B_3 of the superelastic CuAlBe specimen and a Hertzian estimate (dashed line).

Figures 5 and 6 show nanoindentation tests performed on grains B_1, B_2 and B_3 of the CuAlBe specimen. For the three curves the initial loading well matches with elastic contact theory, deviating from the Hertzian estimate with a first displacement burst. For CuAlBe, the elastic Hertzian curves were calculated from the anisotropic reduced modulus. Then, for grains B_1 and B_2, three more excursion events occurduring the loading and the unloading also shows four displacement bursts. For grain B_3 the first excursion event is followed by six pop-in events during loading and seven pop-outs are observed during the unloading. Pop-in and pop-out loads are presented in Table 1 for the three grains. Penetration depth at the end of unloading is almost back to its initial value for grain B_1(the residual strain is around 0.5 nm) and is equal to zero for grains $B_2$and B_3as the final unloading joins back the initial loading (as a typical tensile test of a superelastic CuAlBe at the macroscopic scale).

	Pop-in loads (µN)		Pop-out loads (µN)	
	Grain B_1	Grain B_2	Grain B_1	Grain B_2
1	28	18	22	15
2	48	36	48	35
3	65	49	68	43
4	82	75	76	69

Table 3: Pop-in and pop-out load levels for grains B_1 and B_2 of orientation close to [001]of a superelastic CuAlBe SMA.

	Pop-in loads (µN)	Pop-out loads (µN)
1	55	53
2	125	120
3	175	170
4	300	260
5	360	330
6	400	380
7	420	420

Table 4: Pop-in and pop-out load levels for grains B_3 of orientation close to [111] of a superelastic CuAlBe SMA.

AFM images performed on the SMA indented surface after complete unloading showed no evidence of remnant impressions. This comforts the observation that nanoindentation tests on CuAlBe result with almost complete strain recovery. Then, the observed excursion events on this material are not due to plasticity as in Nickel. However, due to a first displacement burst, the curve deviates from the elastic theory showing an inelastic mechanism. Presence of excursion events during both loading and

unloading and of no residual displacement leads to interpret this inelastic mechanism as reversible phase transformation.
Displacement bursts on the CuAlBe specimen exhibit a slight slope, whereas in Ni the excursion event is clearly a plateau. This difference in the pop-in (and pop-out) slope is thought to be due to the difference in the observed mechanism between dislocation and martensite variant nucleation.
One can see on Table 1 that for the three CuAlBe grains pop-out loads are close from pop-in loads but slightly lower. Thus it seems that at each pop-in during loading corresponds a pop-out during unloading.
The first excursion event (pop-in1) is interpreted as being the activation of the first martensite variant occurring under the indenter. The corresponding pop-out, the last one during unloading (pop-out 1), would then be related to the reverse transformation of this variant from martensite back to austenite.
It can be observed that the length of the following displacement bursts is shorter than the length of pop-in 1. Thus they are assumed not to be due to the same mechanism as the first pop-in. Two assumptions come for this mechanism: reorientation of the first variant or activation of other less active martensite variants. Assuming there is martensite reorientation during loading, the reverse mechanism back to twinned martensite could not occur while performing the test at constant temperature, so this mechanism does not explain the presence of excursion events during unloading. Thus we interpret the displacement bursts 2, 3, 4 (and 5, 6, 7 for grain B_3) as being activation of other martensite variant and the corresponding pop-outs as showing reverse transformation of these variants. These results show the spatiotemporal discontinuity of phase transformation propagation at the nanometer scale.

Nanoindentation curves obtained on grains B_1 and B_2 are pretty similar apart from the maximum load and the load levels of the excursion events. The maximum load was given as an input data before the test and the Hertzian estimate fits very well both of the curves. So the difference between the two achieved maximum loads must be due to a difference in the contact point detection. The load levels of the displacement bursts are approximately 10 µN lower for grain B_2 which orientation is slightly closer from [001] than grain B_1. First of all, the fact that the P-h curves obtained on two grains of close orientation are similar shows the repeatability of the tests and validates the results. Then differences obtained in pop-in and pop-out loads can be explained either by experimental variations or by the large anisotropy of CuAlBe which could lead a small variation in orientation to induce a difference in the activation force.

However the critical load for pop-in activation of B_3 is 55 µN so indisputably greater than for B_1 and B_2, meaning that martensitic transformation requires more energy to be activated in a grain with a [111] orientation than in a grain with a [001] orientation. These experimental results are in good agreement with the indentation Patel and Cohen factors theoretical simulations predicting an easier variant activation on the [001] orientation than on the [111] orientation.

5. Conclusion

Activation of martensitic transformation in a CuAlBe SMA as a function of crystal orientation was investigated in this study. A criterion for the activation of martensitic transformation in SMA under nanoindentation loading is proposed. This indentation Patel and Cohen factor depends on the transformation strain and on the contact stress field, which computation was validated thanks to calculation of the indentation Schmid factor for pure Nickel.
Nanoindentation experiments were performed on pure Nickel and on superelastic CuAlBe SMA. Tests led on Nickel validated our experimental procedure to detect pop-in type discrete mechanisms. Nanoindentation curves of the CuAlBe exhibited complete strain recovery and displacement bursts during both loading and unloading which shows evidence of discrete stress-induced martensitic transformation. Each pop-in is interpreted as the activation of one martensite variant and the corresponding pop-out as the reverse transformation of this variant, showing the discontinuity of phase transformation propagation.
The critical load for the activation of martensitic transformation was found to depend on crystal orientation. Tests performed on a [111] oriented CuAlBe grain showed a greater critical load than tests led on [001] oriented crystals showing a higher indentation Patel and Cohen factor.

As a perspective for this work is the computation of the stress field under hypothesis of anisotropic elasticity and the exploitation of simulation data to predict which martensite variant appears first and the position of its activation under the indenter.
To the knowledge of the present authors, no investigation had been led up to now on the characterization by nanoindentation of martensitic transformation in CuAlBe SMA.

ANNEXE A :
Stress componentsat some arbitrary position (x, y, z) due a concentrated normal point force $p_0$acting on the surface of an elastic half-space (Johnson [20]):

$$\frac{\tilde{\sigma}_{xx}}{p_0} = \frac{1}{2\pi}\left[\frac{(1-2\nu)}{r^2}\left\{\left(1-\frac{z}{\rho}\right)\frac{x^2-y^2}{r^2}+\frac{zy^2}{\rho^3}\right\}-\frac{3zx^2}{\rho^5}\right] \quad \text{(A.1-1)}$$

$$\frac{\tilde{\sigma}_{yy}}{p_0} = \frac{1}{2\pi}\left[\frac{(1-2\nu)}{r^2}\left\{\left(1-\frac{z}{\rho}\right)\frac{y^2-x^2}{r^2}+\frac{zx^2}{\rho^3}\right\}-\frac{3zy^2}{\rho^5}\right] \quad \text{(A.1-2)}$$

$$\frac{\tilde{\sigma}_{zz}}{p_0} = -\frac{3}{2\pi}\frac{z^3}{\rho^5} \quad \text{(A.1-3)}$$

$$\frac{\tilde{\sigma}_{xy}}{p_0} = \frac{1}{2\pi}\left[\frac{(1-2\nu)}{r^2}\left\{\left(1-\frac{z}{\rho}\right)\frac{xy}{r^2}-\frac{xyz}{\rho^3}\right\}-\frac{3xyz}{\rho^5}\right] \quad \text{(A.1-4)}$$

$$\frac{\tilde{\sigma}_{xz}}{p_0} = -\frac{3}{2\pi}\frac{xz^2}{\rho^5} \quad \text{(A.1-5)}$$

$$\frac{\tilde{\sigma}_{yz}}{p_0} = -\frac{3}{2\pi}\frac{yz^2}{\rho^5} \quad \text{(A.1-6)}$$

References

[1] E. Patoor, D.C. Lagoudas, P.B. Entchev, L.C. Brinson, X. Gao, Mech. Mat. 38 (2006) 391-429.
[2] D.F. Bahr, D.E. Kramer, W.W. Gerberich, Acta Mater. 46 (1998) 3605-3617.
[3] W.W. Gerberich, J.C. Nelson, E.T. Lilleodden, P. Anderson and J.T. Wyrobek, Acta Mater. 44 (1996) 3585-3598.
[4] D.J. Morris, S.B. Myers, R.F. Cook, J. Mater. Res. 19 (2004) 165-175.
[5] J. Woirgard, C. Tromas, J.C. Girard, V. Audurier, J. Europ. Cer. Soc. 18 (1998) 2297-2306.
[6] S. Moyne, C. Poilane, K. Kitamura, S. Miyazaki, P. Delobelle, C. Lexcellent, Mat. Sci. Eng. A 273 (1999) 727-732.
[7] A.J. Muir Wood, T.W. Clyne, Acta Mat. 54 (2006) 5607-5615.
[8] M. Arciniegas, Y. Gaillard, J. Peña, J.M. Manero, F.J. Gil, Intermetallics 17 (2009) 784-791.
[9] Y. Zhang, Y.-T.Cheng, D.S. Grummon, J. Appl. Phys 101 (2007).
[10] W.C. Crone, H. Brock, A. Creuziger, Exp. Mech. 47 (2007) 133-142.
[11]H.-S. Zhang, K. Komvopoulos, J. Mater. Sci. 41 (2006) 5021-5024.
[12] X.-G Ma, K. Komvopoulos, J. Mater. Res. 20 (2005) 1808-1814.
[13] C.P. Frick, T.W. Lang, K. Spark, K. Gall, Acta Mater. 54 (2006) 2223-2234.
[14] B. Kaouache, S. Berveiller, K. Inal, A. Eberhardt, E. Patoor, Mat. Sci. Eng. A 438-440 (2006) 773-778.
[15] J. Pfetzing-Micklich, C. Somsen, A. Dlouhy, C. Begau, A. Hartmaier, M.F.-X. Wagner, G. Eggeler, Acta Mat. 61 (2013) 602-616.

[16] J.J. Vlassak, W.D. Nix, J. Mech. Phys. Solids42 (1994) 1223-1245.
[17]G. Simmons, H. Wang, Single Crystal Elastic Constants and Calculated Aggregate Properties: A Handbook, second ed., MIT, Cambridge, 1971.
[18] T.L. Li, Y.F. Gao, H. Bei, E.P. George, J. Mech. Phys. Sol. 59 (2011) 1147-1162.
[19]D. Rios-Jara, A. Planes, Ll. Mañosa, J. Ortin, S. Belkahla, M. Morin, G. Guénin, J.L. Macqueron, J. Phys. IV 1 (1991) 283-288.
[20]K.L. Johnson, Contact mechanics, first edition, Cambridge University Press, Cambridge, 1985.
[21] N. Siredey, E. Patoor, M. Berveiller, A. Eberhardt, Int. J. Sol. Struct. 36 (1999) 4289-4315.
[22] J.R. Patel and M. Cohen, Acta Metall. 1 (1953) 531-538.
[23] S. Shim, H. Bei, E.P. George, G.M. Pharr, Scr. Mater. 59 (2008) 1095-1098.
[24] S.K. Lawrence, D.F. Bahr, H.M. Zbib, J. Mater. Res. 27 (2012) 3058-3066.
[25] J. San Juan, M.L. Nó, C.A. Schuh, Acta Mater. 60 (2012) 4093-4106.
[26] M.S. Wechsler, D.S. Lieberman, T.A. Read, AIME Transcript.197 (1953) 1503-1516.
[27] J. De Vos, E. Aernoudt, L. Delaey, Z. Metallkde 69 (1978) 438-455.
[28]E. Patoor, M ; El Amrani, A. Eberhardt, M. Berveiller, J. Phys. IV 5 (1995) 495-500.